SUPPLEMENTAL DATA

Figure S1: Production and purification of an active form of FBA-tb.

(A) FBA-tb was produced in *E. coli* BL21 DE3/pET29a-*fba-tb* (left panel) and purification was carried out as described under Experimental Procedures. Right panel: The final elution fraction is shown. 10% SDS-PAGE gels stained with Coomassie brilliant blue show large yields of a >90% pure protein at the expected size of 36.5 kDa. An extra-band is noted at 75 kDa, possibly a dimer of the protein.
(B) Principle of the coupled assay used to measure FBA-tb activity and measured FBA-tb activity as a function of the concentration of purified enzyme used in the assay. The reaction mixture was as described under Experimental Procedures. The assay is based on the estimation of triose phosphates (DHAP and G3P) formed from FBP and limiting amounts of the FBA-tb enzyme in the presence of NADH, excess of TIM and GPDH. The triose phosphates formed are converted to glycerol-3-phosphate with the concomitant oxidation of NADH to NAD, which is followed spectrophotometrically at 340 nm. No FBA-tb in the assay (diamonds); no FBP substrate (squares); 0.2 μg ml^{-1} FBA-tb (closed triangles); 0.5 μg ml^{-1} FBA-tb (crosses); 1 μg ml^{-1} FBA-tb (closed circles); 1.5 μg ml^{-1} FBA-tb (open circles).

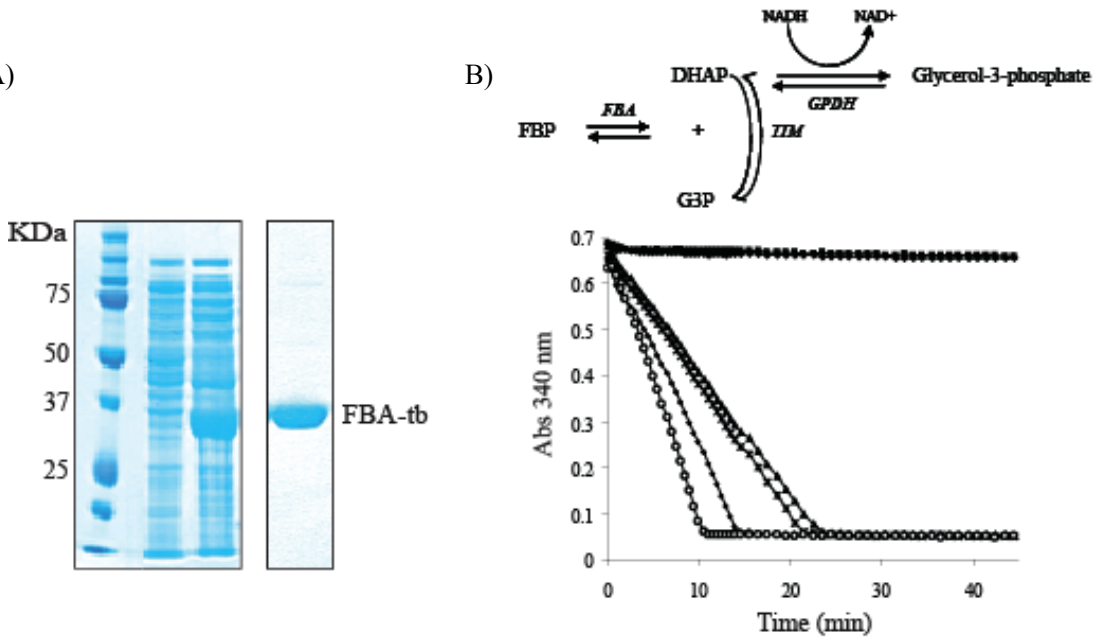

<u>Figure S2</u>: Subcellular distribution of FBA-tb in *M. tb* H37Rv and production of an ortholog of this protein by *M. leprae* bacilli purified from armadillo tissues.

The production of FBA-tb and FBA-leprae in bacterial extracts was detected by immunoblot using rabbit polyclonal anti-FBA-tb antibodies. The bands migrating in the range of 75 kDa possibly correspond to dimers of the protein. (A) *M. tb* immunoblot. Purified FBA-tb (0.2 μg) (lane 1); *M. tb* H37Rv culture filtrate (lane 2); cell wall (lane 3); membranes (lane 4); cytosol (lane 5); whole cell extract (lane 6). 4 μg of proteins were loaded per lane. MWM, molecular weight marker. (B) *M. leprae* immunoblot. 10 μg of proteins were loaded per lane. Cell wall fraction (lane 1); membranes (lane 2); cytosol (lane 3); purified FBA-tb (0.2 μg) (lane 4).

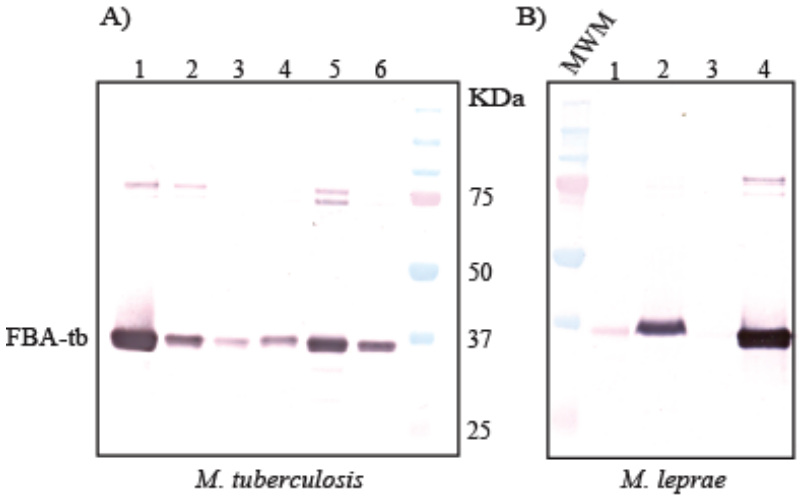

<u>Figure S3</u>: Growth curve of *M. tb* H37Ra grown at 37°C in Sauton with 0.025% tyloxapol and FBA-tb production.

At time points T1 through T4, bacterial cells and culture filtrates were collected and checked for cell lysis by immunoblot using a polyclonal rabbit antibody directed against the cytosolic enzyme PimA (positive signals in the culture filtrates would indicate cell lysis). Immunoblots with FBA-tb antibodies confirmed the presence of the protein in the cells and culture filtrates of all cultures.

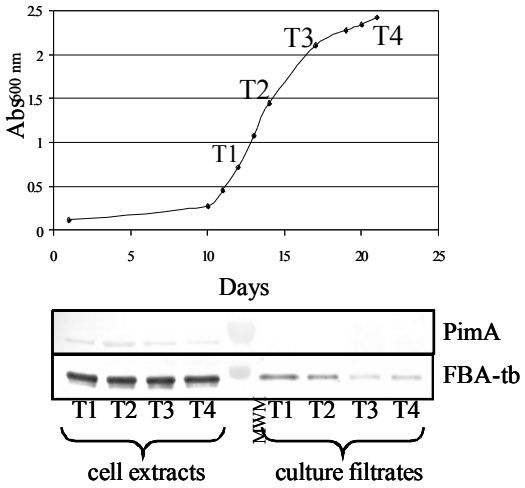

<u>Figure S4</u>: Active site binding of fructose-1,6-bisphosphate (FBP) and TD3 in FBA-tb. Superimposition of FBA-tb in complex with FBP substrate (PDB entry code 3ELF) and FBA-tb in complex with **TD3** indicates coincident binding by **FBP** (orange) and **TD3** (blue) that is consistent with competitive inhibition by **TD3** of the *M. tb* enzyme.

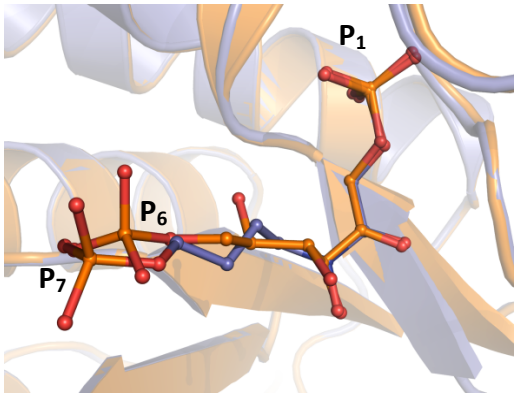

Supplementary Material S5: FBP and TD3 inhibitor binding site prediction by Autodock 4.

Docking simulation - To corroborate the binding site for **TD3** determined in the structure of the FBA-tb-**TD3** complex an alternative approach was pursued based on recent advances of docking calculations that have been successful in predicting binding sites that are in very good agreement with crystallographically determined sites (71-72). In these calculations, the AutoDock (73)-based blind docking approach was used to search the entire surface of proteins for binding sites while simultaneously optimizing the conformations of ligands. The methodology entailed the following: AutodockTools software was used to add polar hydrogen to FBA-tb and Gaisteger charges were then calculated for each atom (74). Affinity grids of 120x120x120 Å with 0.3 Å spacing positioned on the center of mass of the subunit were calculated using autogrid4 for each atom type found in the compounds. Chemical structures for each ligand were converted to PDB format using marvinsketch (74). The script prepare_ligand4.py (ADT utilities) was used to add hydrogen atoms, Gaisteger charges and atom types to each file. Calculations with the phosphate oxyanion utilized the dibasic anion that is the dominant species at pH 8.0. Autodock 4.0 docking calculation used the Lamarckian genetic algorithm (LGA) with population size of 150 individuals, 25 million energy evaluations, a maximum of 27,000 generations, with 1 top individual to survive to the next generation, a mutation rate of 0.02 and a crossover rate of 0.8. The local search probability was set to 0.06 with 300 iterations. Each docking simulation was run 100 times and the resulting conformations clustered using a 2 Å RMSD threshold.

We also performed *in silico* automated docking of FBP-tb with its cognate substrate FBP to cross-check the predictive capability of Autodock 4. In each instance, the binding site predicted for **TD3** and that for FBP, which corresponded to the lowest interaction energy, coincided with the crystallographic determined binding loci **(**Figure **6A** and **6B** respectively), thus substantiating the crystal structure determination of the **TD3** binding site. These results support the capability of the *in silico* docking algorithm to predict ligand binding sites in the *M. tb* aldolase structure.

The partial subunit occupancy by **TD3** afforded an opportunity to estimate the free energy change due to ligand solvation. The salient difference in **TD3** binding in the active site shown in Figure **5** is the solvation of the P7-oxyanion in one subunit (Figure **5A**). The solvation of the oxyanion, even though it reduces the entropy of three water molecules, is concomitant with higher occupancy by **TD3** in this subunit compared to the subunit where the **TD3** P7-oxyanion is not solvated and **TD3** has lower occupancy. This difference in binding affinity of approximately two-fold in **TD3** occupancy corresponds to a net free energy gain in binding energy of ~ 0.4 kcal mol^{-1} that is consistent with computational estimates of free energy gain in other systems sequestering water molecules implicated in inhibitor binding (75). The essentially identical binding mode by **TD3** in both subunits (RMSD 0.72 Å) indicates that the small gain in free energy due to solvation involving hydrogen bonding interactions with three well defined water molecules in one subunit does not alter the interaction of **TD3** with the active site. This result argues that explicit use of water molecules positions in the docking calculations is not required and the good agreement with the prediction of the **TD3** binding site in Figure **6A** supports the use of the computationally efficient implicit solvent model as formulated in the docking calculations (76).

References

71. Hetenyi C. and van der Spoel D. (2006) *FEBS Lett* **580**, 1447-1450
72. Chen Y. and Shoichet BK. (2009) *Nat. Chem. Biol.* **5**, 358-364
73. Morris GM, Goodsell DS, Halliday RS, Huey R, Hart WE, Belew RK. and Olson AJ. (1998) J. Comput. Chem. **19**, 1639–1662.
74. Morris G.M, Huey R. and Olson AJ. (2008) *Curr Protoc Bioinformatics* Chapter **8**, Unit 8-14
75. Hamelberg D, McCammon JA. (2004) *J Am Chem Soc*. **126**, 7683-7689
76. Stouten P, Frommel C, Nakamura H. and Sander C. (1993) *Molecular Simulations* **10**, 97-120.